Journal of Alloys and Compounds 1027 (2025) 180598

Contents lists available at ScienceDirect

Journal of Alloys and Compounds

journal homepage: www.elsevier.com/locate/jalcom

Enhanced strength and ductility in α-titanium alloys through in-situ alloying via additive manufacturing

Xingdong Dan[a,b], Chuanxi Ren[a,b], Dongdong Zhang[a,b], Xuanlai Chen[a,b], Qi Liu[a,b], Hengchao Shi[a,b], K.C. Chan[a,b], Ni Song[c], Dingding Xiang[d], Haoran Sun[e], Zhiyuan Liu[f], Zibin Chen[a,b,*]

[a] *State Key Laboratory of Ultra-precision Machining Technology, Department of Industrial and Systems Engineering, The Hong Kong Polytechnic University, Hong Kong, China*
[b] *Research Institute for Advanced Manufacturing, Department of Industrial and Systems Engineering, The Hong Kong Polytechnic University, Hong Kong, China*
[c] *State Key Laboratory of Powder Metallurgy, Central South University, Changsha 410083, China*
[d] *School of Mechanical Engineering and Automation, Northeastern University, Shenyang 110819, China*
[e] *Koln3D Technology (Medical) Limited, Hong Kong, China*
[f] *Additive Manufacturing Institute, Shenzhen University, Shenzhen 518060, China*

ARTICLE INFO

Keywords:
Additive manufacturing
α-Titanium alloys
Dislocation density
Microstructural evolution
Strength-ductility trade-off

ABSTRACT

Enhancing the strength of titanium alloys through aluminum addition is well-established but often results in significantly reduced ductility. Additive manufacturing (AM) presents a novel approach to fabricating titanium alloys, addressing the persistent challenge of balancing strength and ductility. This study compares the microstructural and mechanical properties of typical Ti-Al alloys produced using conventional casting and AM techniques. The results indicate that, compared to their as-cast counterparts, AM-fabricated Ti-6Al alloys exhibit a remarkable 90 % improvement in yield strength and nearly double the tensile ductility. The enhanced performance of AM alloys is attributed to their refined microstructures, increased dislocation densities, and ultra-high solid solubility, resulting from AM's rapid solidification rates and complex thermal histories. Detailed characterizations reveal that these microstructural features contribute to increased strain hardening and enhanced plastic deformation capacity. This research underscores the potential of AM to revolutionize material properties through microstructural control, providing valuable insights for future alloy design and manufacturing strategies.

1. Introduction

Titanium and its alloys are extensively utilized in aerospace and biomedical applications due to their exceptional strength-to-weight ratio, corrosion resistance, and high-temperature performance [1,2]. Among them, α-titanium (α-Ti) is particularly noteworthy, where the strengthening effects by α-stabilizers such as O, N, and Al are widely established [3–6]. However, while the addition of α-stabilizers enhances the strength of α-Ti, it often significantly reduces ductility, making these alloys less appealing for commercial applications [7]. This challenge is especially pronounced in conventional manufacturing processes such as casting, where intrinsic defects and coarse microstructures further degrade the mechanical tensile ductility, necessitating a series of post-heat treatment processes [8,9].

Additive manufacturing (AM) has recently emerged as a transformative technology capable of overcoming those inherent limitations in conventional methods [10]. Techniques such as laser-by-layer metal deposition have demonstrated the ability to produce alloys with enhanced mechanical properties by leveraging rapid solidification and complex thermal histories [11–15]. These features enable the formation of refined and often non-equilibrium microstructures that are unattainable via conventional processing routes, leading to improved combinations of strength and ductility [16–19]. For instance, Zhang et al. [20] revealed that high-strength low-alloy (HSLA) steels fabricated using wire arc additive manufacturing (WAAM) achieved a higher combination of ultimate tensile strength (σ_{UTS}) of 972.5 MPa and total elongation (ε_{total}) of 17.1 %, surpassing their as-cast counterparts, which exhibited lower strength ($\sigma_{UTS} \sim 778.6$ MPa) and reduced ductility (ε_{total}

---

[*] Corresponding author at: State Key Laboratory of Ultra-precision Machining Technology, Department of Industrial and Systems Engineering, The Hong Kong Polytechnic University, Hong Kong, China.
E-mail address: zi-bin.chen@polyu.edu.hk (Z. Chen).

https://doi.org/10.1016/j.jallcom.2025.180598
Received 24 December 2024; Received in revised form 7 April 2025; Accepted 23 April 2025

~ 10.9 %). Similarly, Avateffazeli et al. [21] observed simultaneous improvements in both strength and ductility in an Al-Cu-Mg-Ag-TiB_2 (A205) alloy produced via laser powder bed fusion (LPBF) compared to its conventionally cast counterparts, attributing these enhancements to the fine equiaxed and supersaturated aluminum grain structures formed under the high cooling rates inherent in the LPBF process. Kang et al. [22] further highlighted the influence of AM techniques on FeMnAlNi alloys, showing that directed energy deposition (DED) yield enhanced ductility while maintaining strength, in contrast to conventional casting counterparts.

In the context of titanium alloys, particularly low-alloyed α-Ti systems, the potential benefits of AM remain underexplored. Traditional methods for introducing alloying elements into titanium typically involve the melting and casting of pre-mixed ingots. These processes often lead to issues such as ingot inhomogeneity, resulting in micro- or macro- segregation [23], as well as β-fleck defects commonly observed in titanium alloys containing Fe or Cr [24]. Furthermore, achieving a homogeneous alloy composition through conventional routes usually requires long-term thermal treatments. These treatments are costly and challenging to apply to titanium alloys due to their high affinity for oxygen and the high diffusion rate of oxygen in the β phase at elevated temperatures [25]. In contrast, in-situ alloying — where elemental powders are blended and alloyed directly during the AM process — offers a more flexible, efficient, and cost-effective alternative for compositional control. This approach allows for real-time control of alloy composition and enables the fabrication of compositionally graded or novel alloy systems that are difficult to achieve through traditional processing [6,26]. Moreover, the rapid solidification inherent to AM processes helps suppress segregation and promotes the formation of refined or metastable microstructures. Although the in-situ alloying approach has demonstrated considerable potential in other alloy systems [27,28], its application to low-alloyed α-Ti alloys remains largely unexplored. Introducing Al via in-situ alloying during AM presents a promising strategy to strengthen α-Ti while retaining or even enhancing ductility, owing to the microstructural control afforded by the process.

This study aims to develop high-performance, low-alloyed α-Ti alloys (Ti-Al) through in-situ alloying using laser engineered net shaping (LENS), a type of DED technique. By systematically comparing the mechanical properties of AM-fabricated Ti-Al alloys with their as-cast counterparts, this work highlights the capability of AM to simultaneously improve both strength and ductility. Notably, the Ti-6 at% Al alloy produced via AM achieved a yield strength (YS) of 795.3 MPa, an ultimate tensile strength (UTS) of 876.1 MPa, and an elongation to failure of nearly 20 %, representing approximately 90 % increase in YS, 80 % increase in UTS, and nearly double the ductility compared to the as-cast counterparts. Detailed microstructural analyses reveal that the superior performance of the AM samples stems from their refined grain structures, elevated dislocation densities, and enhanced solid solubility, all of which result from the rapid solidification and thermal cycling inherent to the AM process. These findings underscore the potential of AM — in combination with in-situ alloying — as a powerful platform for designing next-generation α-Ti alloys with tailored microstructures and optimized mechanical properties, paving the way for their expanded use in high-performance structural applications.

2. Experimental materials and procedures

2.1. Material preparations

2.1.1. Materials

The feedstock powders utilized for AM fabrication include commercially pure titanium (CP-Ti) powder, conforming to ASTM Grade 1 specifications, with a composition of 0.087 % oxygen (O), 0.01 % carbon (C), 0.18 % iron (Fe), and 0.004 % nitrogen (N) (atomic percentage), supplied by Avimetal Powder Metallurgy Technology Co., Ltd. Additionally, pre-alloyed atomized Ti-54Al powder, containing 54.2 % Al, 0.026 % C, and 0.048 % N (atomic percentage), was sourced from Beijing Xing Rong Yuan Technology Co., Ltd. These powders, characterized by a particle size distribution ranging from 50 µm to 103 µm (with a median diameter (D50) of 81.2 µm), demonstrate a spherical morphology and smooth surfaces, which are instrumental in facilitating optimal flowability during the printing process, as depicted in Fig. 1a–c. In preparation for fabrication, the powders were meticulously weighed and homogenized using a powder mixer (Turbula, T2F) at ambient temperature for a duration of 90 minutes, operating at a rotational speed of 200 revolutions per minute, within a sealed container.

2.1.2. LENS fabrication process

The fabrication of bulk Ti-Al samples with Al contents ranging from 0 to 6 at%, and dimensions measuring 35 mm (length) × 16 mm (width) × 3 mm (height), was conducted on a CP-Ti substrate using a LENS system (OPTOMEC LENS™ MR-7). To mitigate oxidation — a critical concern given the sensitivity of titanium and its alloys to oxygen [29] — the build chamber was flushed with high-purity argon gas until the oxygen content was reduced to below 100 parts per million (ppm) before the manufacturing process commenced. The process employed a bidirectional scanning strategy along the X and Y axes, incorporating a 90° rotation after the deposition of each layer to ensure uniformity and structural integrity (Fig. 1d).

To optimize the fabrication parameters, we systematically investigated various combinations of laser power and scanning speed, which are among the most influential parameters in the LENS process. Specifically, scanning speeds of 8 mm/s, 10 mm/s, and 12 mm/s, and laser powers of 300 W, 400 W, and 500 W were evaluated. The printability and formability of the as-fabricated samples were assessed through optical microscopy (OM) on the cross-sectional surfaces. As shown in Fig. 2, the OM images revealed that samples fabricated under the selected conditions exhibited crack-free and nearly pore-free morphologies, indicative of good formability. Based on these results, the optimal processing parameters were determined and are summarized in Table 1.

P, laser power; *T*, layer thickness; *H*, hatch distance; *V*, scanning speed; FOP 1, feed rate of powder.

2.1.3. Conventional as-cast method

For comparative analysis, alternative fabrication methods were employed to produce reference samples of as-cast Ti-6Al, maintaining identical elemental compositions to those of the samples fabricated by AM. These reference specimens were crafted using high-purity Ti and Al ingots (99.99 % purity) through a process of arc melting followed by water-cooled copper-mold casting. To ensure minimal oxygen presence, the arc melting chamber was first evacuated to a pressure of 5×10^{-3} Pa, then backfilled with argon gas to a pressure of 0.5 Pa prior to melting. The Ti and Al ingots were melted seven times to achieve a homogeneous distribution of alloying elements and mitigate the presence of unmelted sections within the as-cast sample. Subsequently, the resulting molten ingot, conforming to the Ti-6Al alloy composition, was solidified within a cavity of a water-cooled copper mold. The elemental composition of the resulting reference samples was verified to be consistent with the designed alloy, as confirmed by subsequent Energy Dispersive Spectroscopy (EDS) analysis.

2.2. Mechanical performance evaluation

Tensile testing specimens, derived from both the as-cast and LENS-fabricated samples, were shaped into a dog-bone configuration using a wire-cut electric discharge machine (WEDM), with specifications of 2 mm in gauge diameter, 10 mm in gauge length, and an overall length of 25 mm. The evaluation of their room temperature tensile properties was conducted using a ZwickRoell Z020 TEW universal testing machine at a constant strain rate of 1×10^{-3} s^{-1} . Elongation was measured using a laser-based optical extensometer (ZwickRoell laserXtens 1–32 HP/TZ), which tracks the displacement of laser-induced speckle patterns via

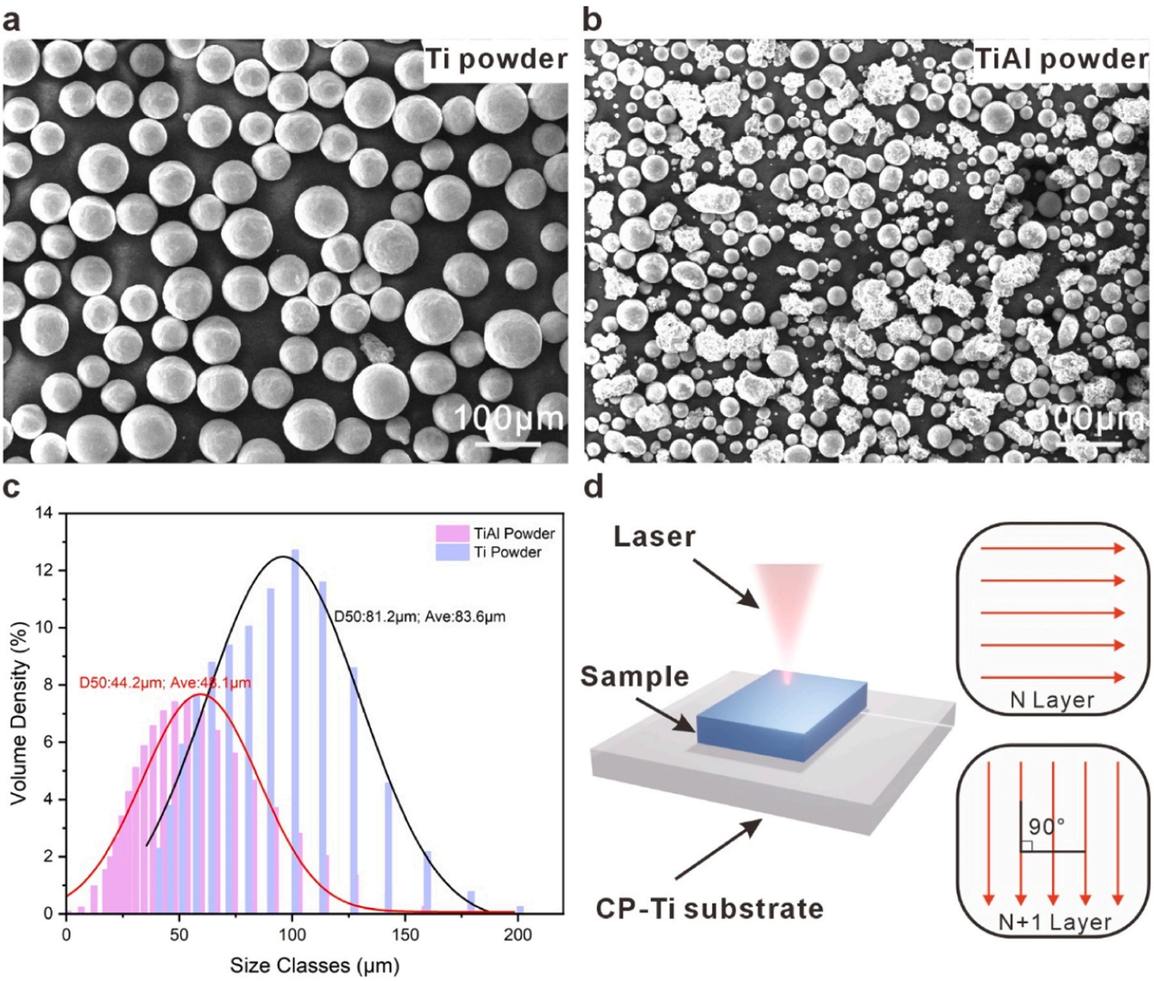

Fig. 1. Materials and printing strategies utilized in this study. (a, b) Morphologies of pure Ti and pre-alloyed TiAl powders. (c) Particle size distribution of pure Ti and pre-alloyed TiAl powders. (d) Printing strategies for consecutive layer deposition.

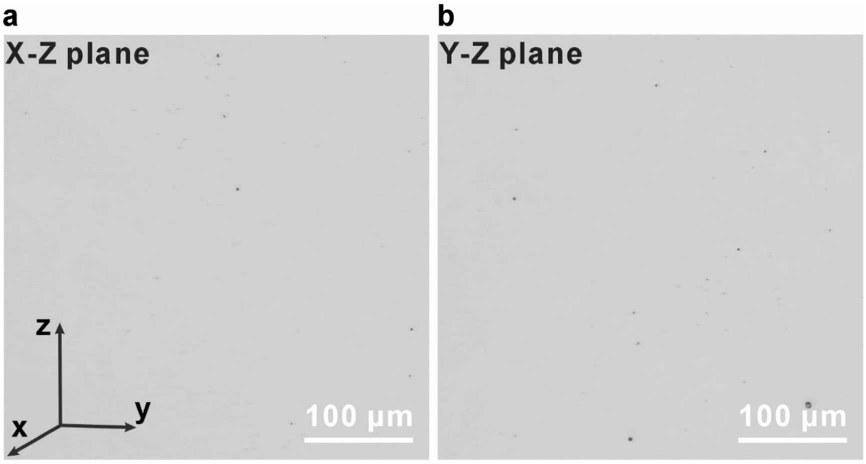

Fig. 2. OM images showing the cross-sectional morphologies of the as-fabricated Ti-x at%Al samples produced by LENS under the optimized processing parameters, exhibiting nearly pore-free morphologies. (a) Cross-section along the X-Z plane; (b) Cross-section along the Y-Z plane.

digital image correlation (DIC). Three specimens from each fabrication method were tested to ensure repeatability and reliability.

Table 1
The process parameters of LENS™ fabricated Ti-6Al.

Parameters	P (W)	T (μm)	H (μm)	V (mm/s)	FOP (g/s)
AM Ti−6Al	400	100	300	10	0.2

2.3. *Microstructure characterization*

The characterization of phase constituents within the as-cast and

LENS-fabricated specimens was conducted using X-ray diffraction (XRD) analysis with a Rigaku SmartLab 9 kW system. XRD measurements were performed at a scan rate of 5° min^{-1} and a step size of 0.02°, covering a diffraction angle (2θ) range from 20° to 90°.

Microstructural examinations of the specimens were conducted using an Olympus B53X optical microscope (OM) and a Tescan Mira scanning electron microscope (SEM) equipped with EDS. For the LENS-fabricated sample, cross-sections aligned parallel to the build direction (Z-direction) were meticulously prepared through WEDM, followed by standard metallurgical grinding and polishing processes. These prepared surfaces were etched using Kroll's reagent (comprising 3 % hydrofluoric acid, 6 % nitric acid, and water) for 10 seconds to enhance microstructural visibility during subsequent OM and SEM analyses.

Further crystallographic characterization was conducted using a ZEISS Gemini 300 SEM equipped with an electron backscatter diffraction (EBSD) detector. Sample preparation for EBSD involved a series of mechanical grinding and polishing steps, concluding with electropolishing in a solution with a volumetric ratio of $HClO_4$:$C_4H_{10}O$:CH_4O (6:34:60), performed at a current of 0.4 A and a temperature of −20°C. Additionally, a JEOL JEM-2100F transmission electron microscope (TEM), capable of operating in both TEM and scanning TEM (STEM) modes at an acceleration voltage of 200 kV, was employed to investigate the microstructure at the nano- and atomic scales. Preparation of TEM specimens involved initial mechanical thinning to approximately 30 μm, followed by precision thinning using a Gatan precision ion polishing system II (PIPS II). The ion milling was executed using sequential beam voltages of 5 kV, 3 kV, and 1 kV, with milling angles set at ± 7°, ± 5°, and ± 5° for the rough milling, fine milling, and final cleaning stages, respectively.

3. Results

3.1. Mechanical performance

The mechanical properties of Ti alloys fabricated using conventional methods, such as casting or forging, with small additions of Al — typically less than 10 at%Al without the presence of the α_2 phase — have been thoroughly investigated and well-documented [8,30,31]. These studies consistently show that increases in Al content, ranging from 0 to 6 at%, result in strength enhancement but come at the cost of significant reductions in ductility. In comparison, the engineering tensile stress--strain behavior of the AM Ti-x at%Al alloys was evaluated, as presented in Fig. 3a. Notably, the AM commercially pure titanium (CP-Ti) demonstrated the highest uniform elongation but correspondingly exhibited the lowest strength. As the Al content increased, the strength of the alloys improved while the ductility decreased. Among the various Al concentrations, the AM Ti-6 at%Al (hereafter referred to as AM Ti-6Al) sample displayed the most favorable combination of strength and ductility, with a yield strength (YS) of 795.3 MPa and an ultimate tensile strength (UTS) of 876.1 MPa, accompanied by a remarkable elongation to failure (ε_f) of nearly 20 %.

For comparative purposes, a Ti-6 at%Al sample fabricated via casting (hereafter referred to as as-cast Ti-6Al) was also produced and tested, showing a YS of 417.2 MPa, UTS of 492.7 MPa, and ε_f of only 10.8 %, consistent with previously reported data [8,32]. Analysis of the strain hardening rate–true strain curves (Fig. 3b) derived from the stress–strain curves further revealed a significantly higher strain-hardening rate and greater true strain values in the AM Ti-6Al sample compared to its as-cast counterpart. These findings underscore the superior mechanical performance achieved through AM for low-alloyed Ti-Al alloys.

3.2. Microstructure analysis

While both the AM and casting processes introduce Al into Ti with identical compositions, the TiAl alloys produced by AM consistently demonstrate superior mechanical properties, including enhanced strength and ductility, compared to the as-cast counterpart. This discrepancy suggests that the distinct microstructural evolution resulting from the different fabrication techniques plays a critical role in determining the mechanical performance of the alloys. To further investigate the microstructural mechanisms responsible for this enhanced performance, a detailed analysis was conducted, focusing on the AM Ti-6Al sample with the optimal combination of strength and ductility, as well as its as-cast Ti-6Al counterpart. The following section presents an in-depth microstructural examination to elucidate how processing-induced features contribute to the observed differences in mechanical behavior.

3.2.1. Phase constituents

Fig. 4 presents the phase constituents of CP-Ti, pre-alloyed Ti-54 at% Al powders (hereafter referred to as Ti-54Al powder) used in the AM process, and both as-cast and AM Ti-6Al samples. Consistent with the Ti-Al phase diagram [33], the results show that CP-Ti powder contains only the α-Ti phase, while the Ti-54Al powder exhibits both the α_2-Ti_3Al and γ-TiAl phases. In examining the as-fabricated Ti-6Al samples from cross-sectional surfaces parallel to the build direction, it was found that both the as-cast and AM samples primarily consist of the α-Ti phase. Notably, neither the α_2-Ti_3Al and γ-TiAl phases were detected in the AM

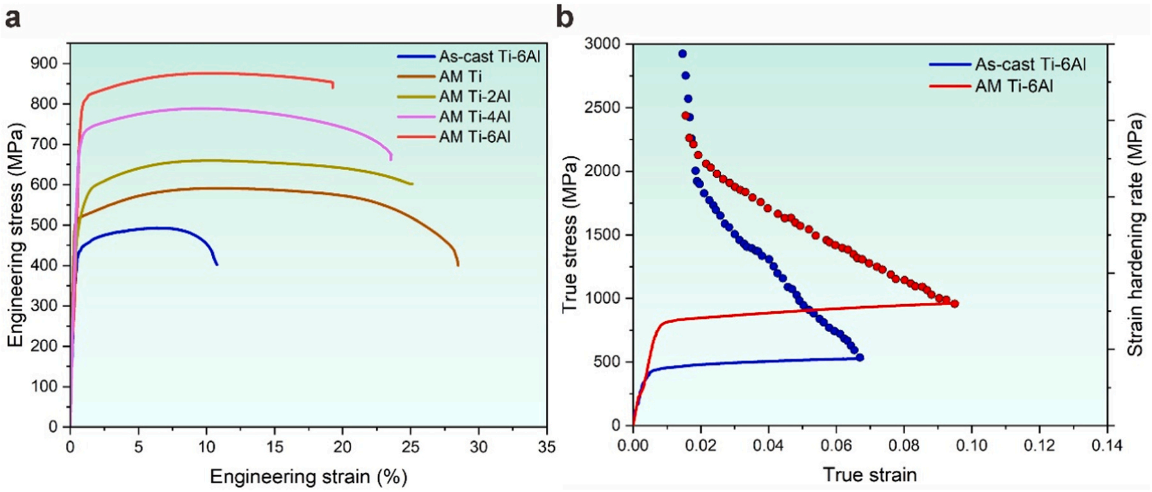

Fig. 3. Mechanical properties of as-cast Ti-6Al and AM Ti-x at%Al alloys. (a) Engineering stress–strain curves for as-cast Ti-6Al and AM Ti-x at% Al samples. (b) True stress–true strain curves and strain-hardening rate curves for as-cast and AM Ti-6Al alloys.

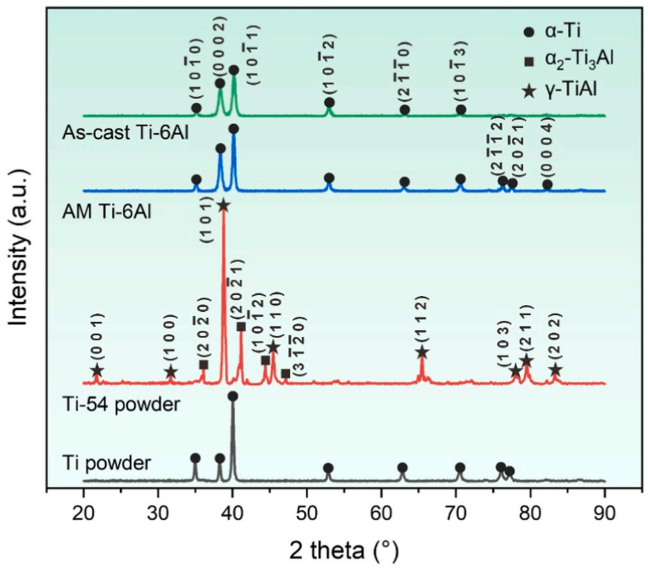

Fig. 4. Phase analysis of pure Ti and pre-alloyed Ti-54 at%Al powders, and Ti-6Al samples fabricated by casting and AM methods.

samples made from CP-Ti and Ti-54Al powders, indicating effective melting and homogeneous mixing during the AM process. Furthermore, a noticeable shift of XRD peaks towards higher angles in both as-cast and AM Ti-6Al samples, compared to the CP-Ti powder, indicates lattice distortion induced by the solid solution of Al in Ti, suggesting effective alloying in both manufacturing process [34].

3.2.2. Microstructure observations

Fig. 5 illustrates the microstructural characteristics of the as-cast and AM Ti-6Al samples as observed through OM and SEM. The OM images of the as-cast Ti-6Al samples (Fig. 5a1–a2) reveal a microstructure predominantly composed of uniformly distributed α-grains with large plate-like morphologies, interspersed with long, parallel α-columnar grains. This morphology is characteristic of the slow cooling rate associated with the β to α phase transformation in titanium alloys [35]. Higher magnification SEM images (Fig. 5a3) further confirm this microstructure, revealing prominently oriented α-columnar grains embedded within the larger plate-like grains. Complementary EDS mapping (Fig. 5a4–a5) indicates a relatively uniform distribution of Ti and Al elements, with Al concentrations consistently maintained at around 6 at %, demonstrating homogeneity throughout the sample.

In contrast, the microstructure of the AM Ti-6Al samples shows significant differences. The OM images (Fig. 5b1–b2) show a more refined grain structure, characterized by a predominantly uniform distribution of coarse α-grains with smaller plate-like morphologies. Additionally, these α-grains are adorned with smaller quantities of finer α-grains displaying basketweave morphologies, likely resulting from the rapid solidification rates inherent to the AM process. The corresponding SEM images and EDS mapping (Fig. 5b3–b5) provide further insights into the fine basketweave α-grains, which measure only a few micrometers in size, and confirm a uniform elemental distribution. The concentration of Al remains consistent at approximately 6 at%, similar to that of the as-cast samples. The absence of elemental segregation suggests that the observed microstructural differences are primarily attributable to the distinct thermal histories and solidification dynamics associated with the two fabrication methods, rather than compositional inconsistencies during processing.

3.2.3. Crystallographic analysis

To better investigate the microstructural differences in these samples, a comprehensive crystallographic analysis was performed using EBSD measurements, with the results presented in Fig. 6. In the as-cast Ti-6Al sample (Fig. 6a1), the inverse pole figure (IPF) map reveals large plate-like grains with no significant textural orientation. These grains are interspersed with columnar α-grains exhibiting low levels of intragranular misorientation, consistent with previous findings [36]. Quantitative grain size analysis (Fig. 6a2) reveals that the average grain size of the large plate-like α-grains is approximately 229.1 ± 59.9 μm,

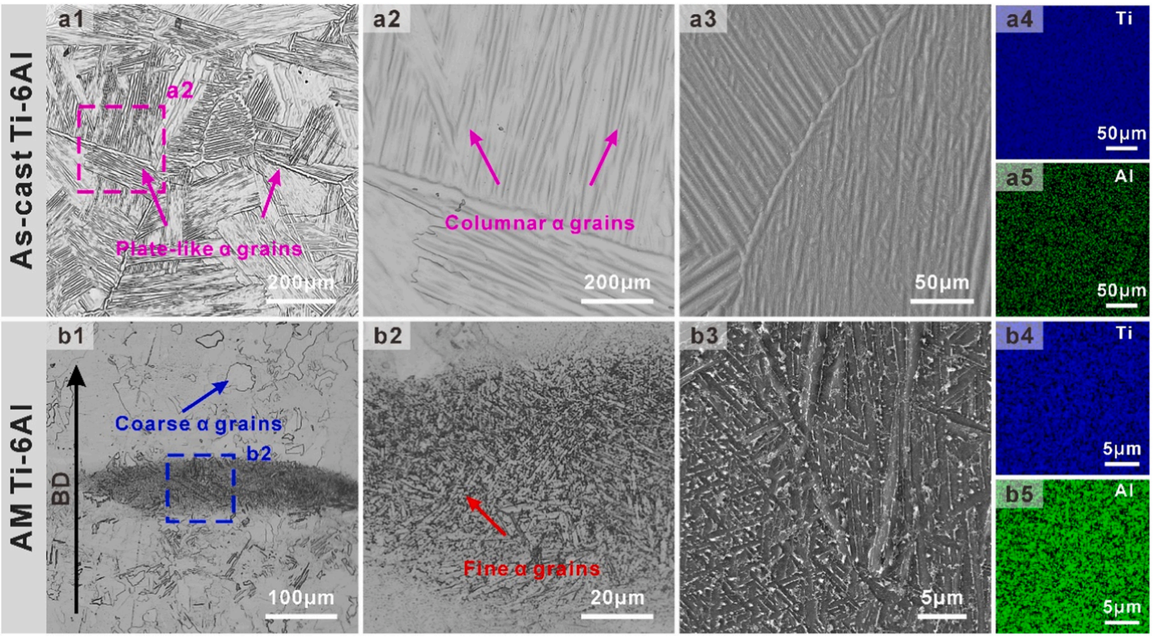

Fig. 5. Microstructural analysis of as-cast and AM Ti-6Al samples. (a1, a2) OM images of as-cast Ti-6Al samples show large, plate-like α-grains interspersed with parallel α-columnar grains. (a3) Higher magnification SEM image showing prominently oriented columnar grains embedded within the plate-like grains. (a4, a5) EDS mapping confirms uniform distribution of Al and Ti. (b1, b2) OM images of AM samples display coarse α-grains with finer plate-like and basketweave morphologies. (b3) Higher magnification SEM image reveals the appearance of finer basketweave grains measuring only a few micrometers. (b4, b5) EDS mapping shows uniform Al and Ti distribution.

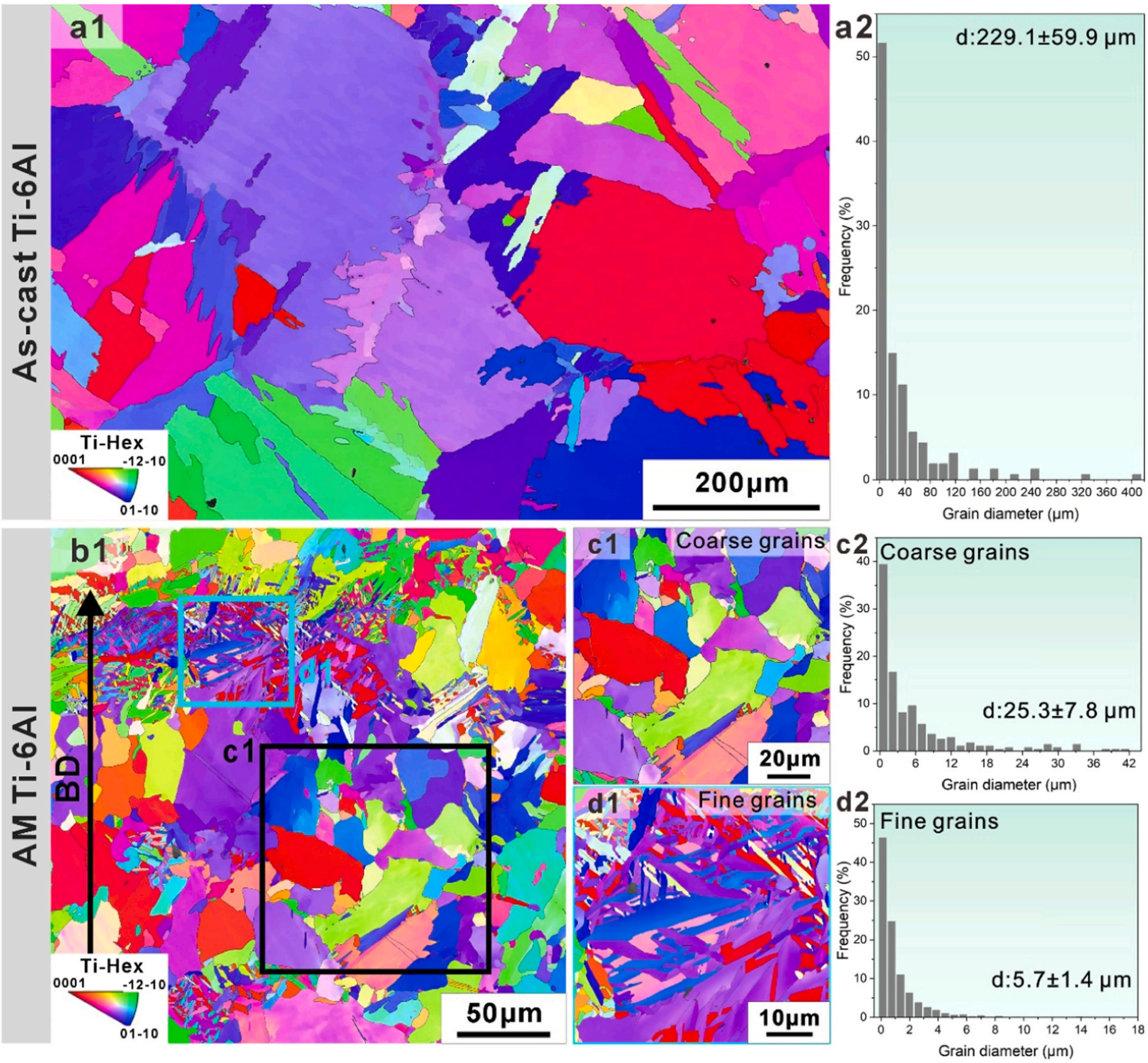

Fig. 6. EBSD analysis of the as-cast and AM Ti-6Al samples. (a1) IPF map of the as-cast sample, showing large plate-like grains with minimal textural orientation. (a2) Statistical analysis quantifying the average grain size of the large plate-like α-grains, measured at 229.1 ± 59.9 μm. (b1) IPF map of the AM sample, highlighting coarse plate-like grains (dark square) and finer basketweave grains (blue square). (c1, d1) Higher magnification views of the coarse and fine grains, respectively. (c2, d2) Grain size distribution of the coarse and fine grains, measured at 25.3 ± 7.8 μm and 5.7 ± 1.4 μm, respectively.

providing a clear statistical representation of the grain structure in the as-cast sample. The relatively large standard deviation observed is attributed primarily to variations in local nucleation density and inherent cooling-rate inhomogeneities associated with the casting process [37].

In contrast, the EBSD analysis of the AM Ti-6Al sample demonstrates a significantly refined microstructure, predominantly composed of coarse plate-like grains, which occupy approximately 75 % of the observed area. These grains, marked by dark squares in Fig. 6b1 and further magnified in Fig. 6c1, have a considerably smaller average grain size of 25.3 ± 7.8 μm, as quantified in Fig. 6c2. Additionally, fine basketweave grains constituting approximately 25 % of the observed microstructure (highlighted by blue squares in Fig. 6b1 and further detailed in Fig. 6d1) exhibit an even smaller average grain size of 5.7 ± 1.4 μm, as shown quantitatively in Fig. 6d2. Due to the rapid and uniform solidification rates characteristic of the AM process, the grain size distributions in the AM samples exhibit markedly lower standard deviations compared to their as-cast counterparts. In the meanwhile, similar to the as-cast sample, the AM Ti-6Al sample does not display any pronounced textural orientation, consistent with previously reported observations for AM titanium alloys [38].

Considering the substantial impact of fabrication methods on grain size and morphology, as previously discussed, in-depth assessments of Kernel Average Misorientation (KAM) maps and geometric necessary dislocation (GND) densities were performed for both the as-cast and AM Ti-6Al samples, as depicted in Fig. 7. In the as-cast Ti-6Al alloys (Fig. 7a1–a2), the KAM map reveals pronounced local misorientations near sub-GBs and GBs. The corresponding GND density map indicates a relatively uniform distribution of dislocations within the large plate-like grains, with slightly elevated GND densities localized along GBs. Statistical analysis in Fig. 7a3 shows an average GND density of approximately (1.29 ± 0.06) × $10^{14}/m^2$, measured across multiple regions in the as-cast Ti-6Al sample.

In contrast, the AM Ti-6Al sample (Fig. 7b1-b2 and c1-c2) exhibits different characteristics. Although the KAM maps reveal a generally uniform distribution across the matrix, with higher misorientations near boundaries, the distribution of GND densities varies across different regions. In the coarse-grain regions, GND densities exhibit a relatively uniform distribution with an average value of approximately (4.45 ± 0.24) × $10^{14}/m^2$ (Fig. 7b3). However, in the finer basketweave grain regions, the GND densities increased significantly, reaching an average of approximately (17.88 ± 0.18) × $10^{14}/m^2$ (Fig. 7c3). This substantial increase is attributed primarily to the rapid solidification rates and unique thermal history inherent to the AM process, which not only

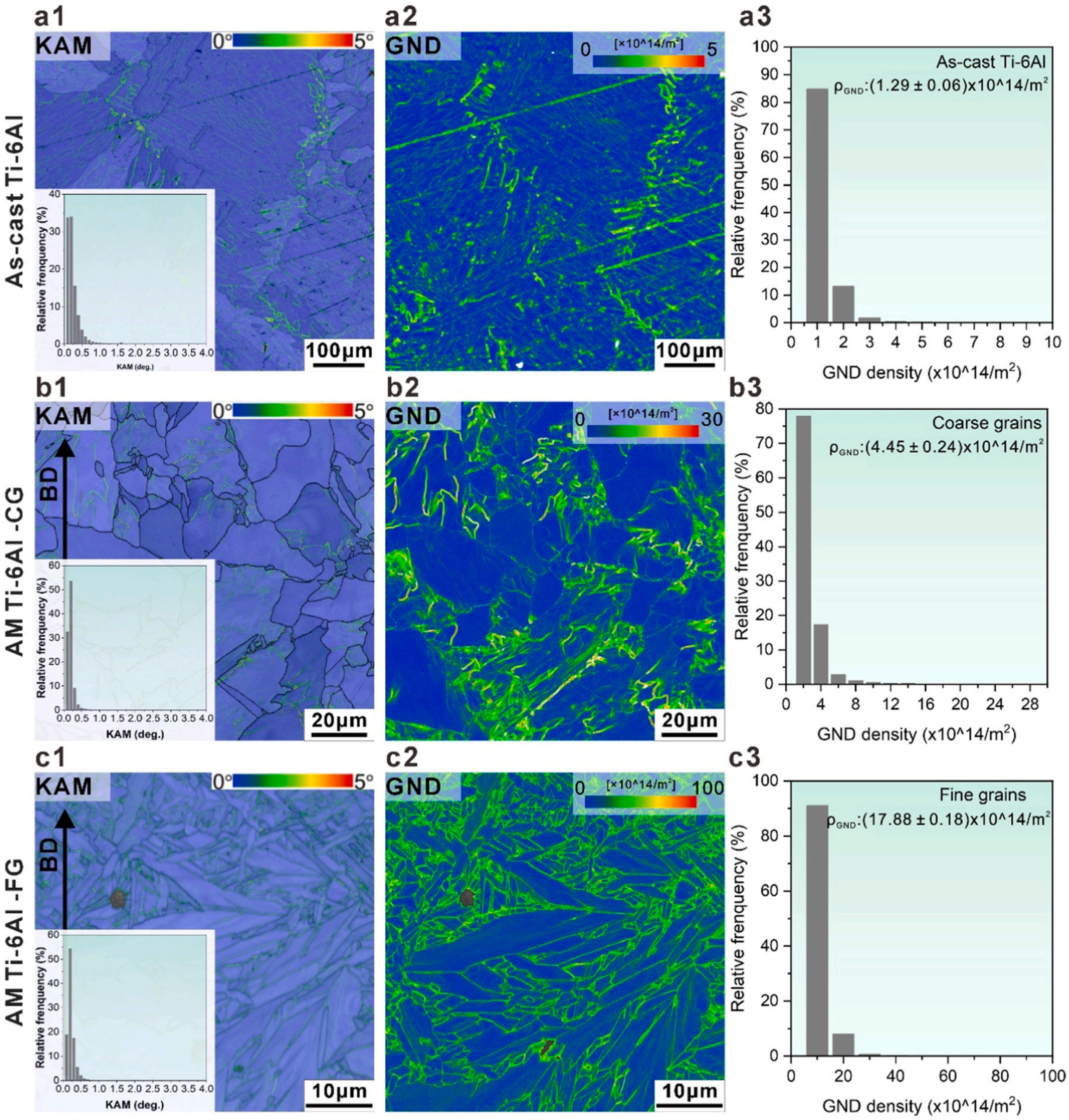

Fig. 7. In-depth analysis of KAM and GND densities in as-cast and AM Ti-6Al samples. (a1-c1) KAM maps illustrate local misorientations in the as-cast Ti-6Al sample, coarse grains, and fine grains in the AM Ti-6Al sample, respectively. Inset images show histograms of local misorientation distribution along with average KAM values. (a2-c2) Corresponding GND density maps highlighting the spatial distribution of dislocation densities across the regions. (a3-c3) Quantitative analyses of GND density, detailing the average dislocation densities for the as-cast Ti-6Al sample and for the coarse and fine grains in the AM Ti-6Al samples.

refines the grain structure but also promotes the generation and accumulation of higher dislocation densities, particularly within finer-grained regions.

4. Discussions

4.1. Strengthening mechanisms

The tensile testing results (Fig. 3) indicate that the AM Ti-6Al sample demonstrates significantly enhanced mechanical properties, achieving an exceptional combination of ultrahigh strength and improved ductility compared to the as-cast counterpart. While the distinct microstructures resulting from the different manufacturing processes have been thoroughly characterized in the previous sections, it is essential to further elucidate the contributions of various strengthening mechanisms that arise from these microstructures and influence the yield strength (σ_y) of the AM Ti-6Al sample relative to the as-cast Ti-6Al alloy.

The yield strength of both the as-cast and AM Ti-6Al samples is expressed as the sum of contributions from individual strengthening mechanisms. These include the critical resolved shear stress of pure Ti (σ_{CRSS}) [39], solid solution strengthening due to Al addition (σ_{ss}), dislocation strengthening (σ_ρ), and grain boundary strengthening (σ_{GB}). Assuming that these mechanisms follow a linear mixture, the overall yield strength can be described by the following equation [40,41]:

$$\sigma_y = \sigma_{CRSS} + \sigma_{ss} + \sigma_\rho + \sigma_{GB} \tag{1}$$

Given that the Al concentration remains consistent at 6 at% for both the as-cast and AM Ti-6Al samples, as evidenced in Fig. 5, it is reasonable to assume that the critical resolved shear stress of pure Ti (σ_{CRSS}) and the solid solution strengthening effect (σ_{ss}) are equivalent for both samples. Therefore, the observed increase in yield strength of the AM Ti-6Al sample compared to the as-cast Ti-6Al sample can be attributed primarily to other strengthening mechanisms. This increment in yield strength can be expressed as:

$$\sigma_{increment} = \Delta\sigma_{\rho} + \Delta\sigma_{GB} \tag{2}$$

Here, the $\Delta\sigma_{\rho}$ represents the dislocation strengthening due to increased dislocation density in the AM sample, and $\Delta\sigma_{GB}$ accounts for the extra grain boundary strengthening resulting from refined grain sizes in the AM sample.

Additionally, based on the EBSD analysis (Figs. 6 and 7), the microstructure of the AM Ti-6Al sample is composed of two distinct grain structures: predominantly coarse plate-like α grains and a smaller fraction of finer basketweave α grains, along with varying dislocation densities. Therefore, considering the rule of mixtures for composite materials comprising two components, the yield strength of the AM Ti-6Al sample can be determined as [42,43]:

$$X = f_{fine}X_{fine} + f_{coarse}X_{coarse} \tag{3}$$

Where X is the composite yield strength, X_{fine} and X_{coarse} are the yield strengths of the individual components, and f_{fine} and f_{coarse} are their respective volume fractions. In the AM Ti-6Al sample, the volume fractions of the coarse and fine grains are 75 % and 25 %, respectively. Thus, the Eq. (2) can be further expanded as:

$$\sigma_{increment} = f_{fine} \quad (\Delta\sigma_{\rho-fine} + \Delta\sigma_{GB-fine}) + \quad f_{coarse} \quad (\Delta\sigma_{\rho-coarse} + \Delta\sigma_{GB-coarse}) \tag{4}$$

Here, the individual parameter σ_{ρ} is attributed to dislocation hardening, described by the Taylor hardening model [44]:

$$\sigma_{\rho} = aM\mu b\sqrt{\rho} \tag{5}$$

Where a is the dislocation interaction constant (0.2 for α-Ti [45]), μ is the shear modulus (44 GPa for α-Ti [46]), M is the Taylor factor (1 for α-Ti [39]), b is the Burgers vector (0.290 nm [44,47]), and ρ is the dislocation density that can be calculated by the following equation [48, 49]:

$$\rho = \frac{2\theta_{KAM}}{X_{step}b} \tag{6}$$

Here, X_{step} represents the EBSD scanning step size, which varies across the samples and regions, with values of 1μm for as-cast Ti-6Al, 0.15 μm for coarse-grain AM Ti-6Al, and 0.03 μm for fine-grain AM Ti-6Al sample. The parameter θ_{KAM} denotes the average local misorientation, obtained from EBSD statistics (Fig. 7a1-c1), and is calculated from the following expression:

$$\theta_{\mathrm{KAM}} = \exp\left[\frac{1}{N}\Sigma_1^i InKAM_{L,i}\right] \tag{7}$$

Where $KAM_{L,i}$ is the local KAM value at point t i, and N represents the total number of points within the test area [50].

Based on these parameters, the strength increments due to dislocation hardening in the AM sample are calculated as 103 ± 19 MPa for coarse grains ($\Delta\sigma_{\rho-coarse}$) and 391 ± 23 MPa for fine grains ($\Delta\sigma_{\rho-fine}$).

Similarly, grain boundary strengthening due to grain refinement can be calculated using the Hall-Petch relation [51]:

$$\sigma_{H-P} = k_{H-P} \bullet d^{-1/2} \tag{8}$$

Where d is the average grain size derived from SEM and EBSD statistics (Figs. 5 and 6), and k_{H-P} is the Hall-Petch coefficient for Ti alloys, ranging from 0.5 to 0.7 MN $\bullet\, m^{-3/2}$ [52], with a value of 0.6 MN $\bullet\, m^{-3/2}$ used for simplicity. Applying this equation, the grain boundary strengthening increments, relative to the as-cast sample, are calculated as 94 ± 22 MPa for coarse grains ($\Delta\sigma_{GB-coarse}$) and 240 ± 40 MPa for fine grains ($\Delta\sigma_{GB-fine}$).

Based on the equations and values provided, the strengthening increments from both dislocation and grain boundary mechanisms in the coarse and fine grains of the AM Ti-6Al sample, relative to the as-cast counterpart, have been thoroughly quantified and are presented in Fig. 8. The total strength increment for the AM Ti-6Al sample is calculated to be 329 ± 25 MPa. When combined with the yield strength of the as-cast sample, the theoretical yield strength of the AM sample is predicted to be 759 ± 30 MPa, which closely aligns with the experimentally measured value of 802 ± 10 MPa. This strong correlation between theoretical and experimental results highlights the significant strengthening effect achieved through additive manufacturing, primarily due to rapid solidification and microstructural refinement compared to the as-cast counterpart.

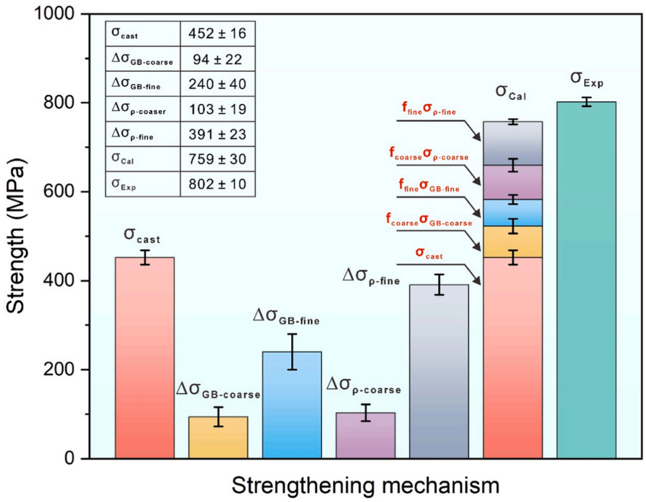

Fig. 8. Contributions of individual strengthening mechanism to the yield strength increment in the AM Ti-6Al sample compared to the as-cast Ti-6Al counterpart.

4.2. Origin of good ductility in the AM Ti-6Al sample

One of the most noteworthy findings of this study is the enhanced ductility of the AM Ti-6Al sample, achieved alongside increased strength, in comparison to the as-cast Ti-6Al sample. It is well established that improvements in strength are typically accompanied by a reduction in ductility [53,54]. To investigate the underlying mechanisms responsible for the superior ductility in the AM Ti-6Al sample, a detailed analysis of the microstructure prior and after deformation was conducted, with the examination divided into two sections.

4.2.1. Dislocation behaviors

An in-depth TEM analysis was performed on both the as-cast and AM Ti-6Al samples before deformation and after fracture, as shown in Fig. 9. In the as-cast sample (Fig. 9a and b), high-density dislocation arrays with a pronounced criss-cross morphologies are observed throughout the matrix. These dislocations are predominantly long and straight, with limited dislocation activity observed beyond these pile-ups, indicative of restricted cross-slip and a tendency toward planar slip. Such planar slip behaviors, including dislocation pile-ups and localized deformation, are widely reported in α-titanium alloys containing aluminum additions and are typically associated with short-range ordering (SRO) [55,56]. Previous studies have extensively documented that aluminum-induced SRO in as-cast Ti-Al alloys promotes a transition from wavy to planar slip, allowing dislocations to glide continuously along specific atomic planes and thus resulting in localized slip behaviors. This localization reduces the size of plastic deformation zones near fatigue crack tips, ultimately leading to a reduction in both ductility and fracture toughness [57–59]. Consequently, as macroscopic strain accumulates, planar slip can induce strain softening, influencing the overall mechanical response of the material [60,61].

In contrast, the as-built AM Ti-6Al samples exhibit a high density of curved dislocations uniformly distributed within the grains, as shown in

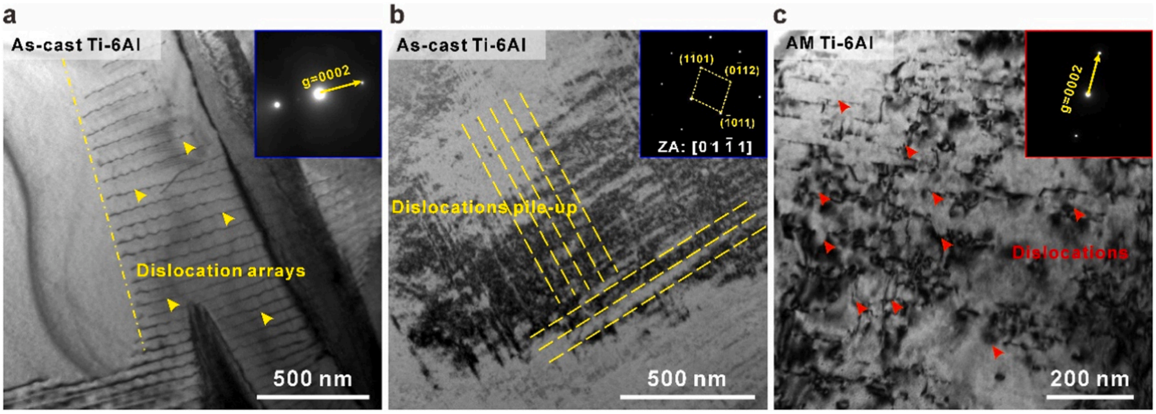

Fig. 9. Microstructural features of as-cast and AM Ti-6Al samples before deformation. (a, b) Bright-field TEM (BF-TEM) images of the as-cast Ti-6Al sample, showing dislocation pile-up configurations within the α-matrix. (c) BF-TEM image of the AM Ti-6Al sample, displaying predominantly curved dislocation configurations within the α-matrix.

Fig. 9c. Unlike the casting process, which involves slow cooling, the rapid cooling rates in AM promote the formation of a supersaturated solid solution, as widely documented in the literature [62,63]. This rapid solidification prevents Al segregation, thereby suppressing the formation of SRO. As a result, the absence of SRO enables dislocations to propagate more freely within the matrix, allowing for greater dislocation mobility and interaction, which accommodates plastic deformation more effectively [64].

The deformation behavior of both as-cast and AM Ti-6Al samples was further investigated through microstructural examination of the fractured samples, as shown in Fig. 10. In the as-cast Ti-6Al sample, deformation was dominated by planar slip, characterized by well-organized dislocation arrays that formed localized deformation zones (Fig. 10a and b). These planar slip bands restrict cross-slip and dislocation

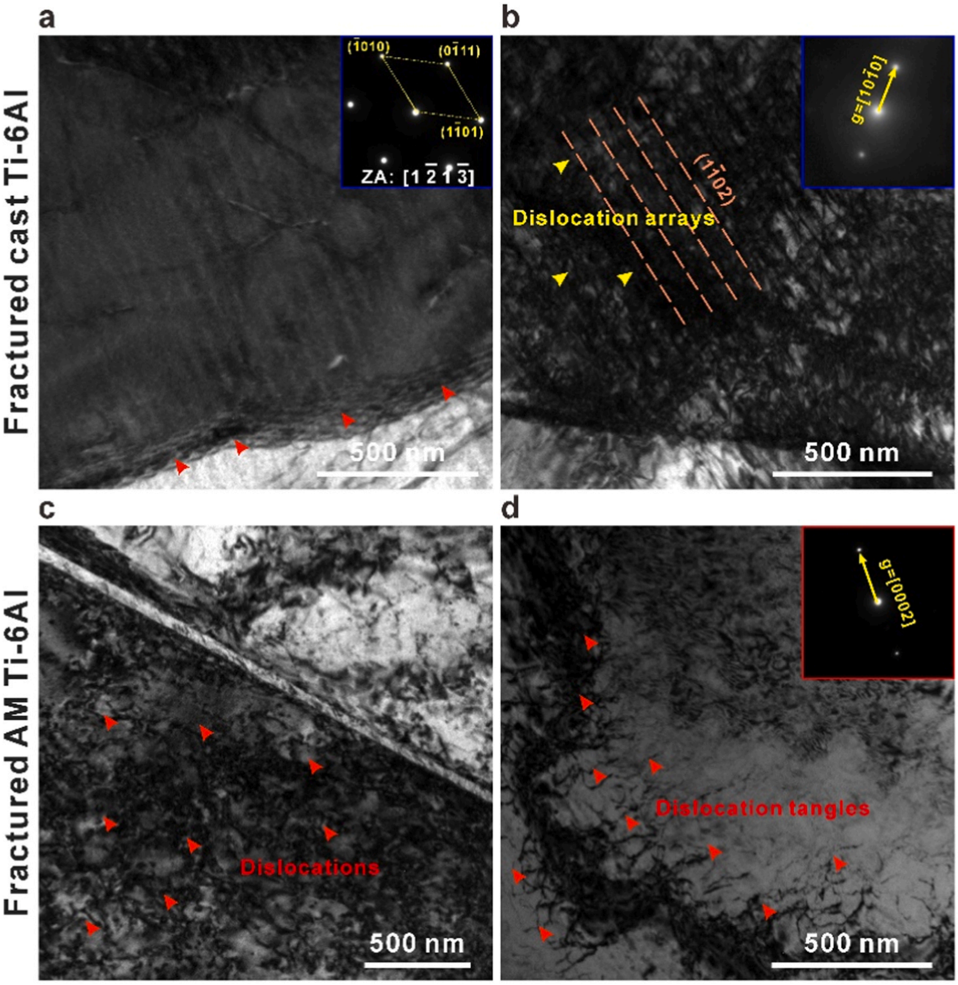

Fig. 10. Microstructural features of as-cast and AM Ti-6Al samples after fracture. (a, b) The BF-TEM images revealing dislocation configurations in the as-cast Ti-6Al sample after fracture. (c, d) The BF-TEM images showing dislocation configurations in the AM Ti-6Al sample post-fracture.

interactions, resulting in a rapid decline in strain-hardening capability and limited elongation prior to fracture. This behavior is typical of conventionally cast Ti alloys, where solute segregation and coarse microstructures promote embrittlement and impede dislocation mobility [24].

In contrast, the AM Ti-6Al sample reveals a high density of curved and entangled dislocation segments (Fig. 10c and d), reflecting significantly enhanced dislocation activity and strain-hardening capacity. This behavior arises primarily due to the absence of SRO, which facilitates dislocation mobility, encourages interactions among dislocations, and promotes activation of Frank-Read sources for dislocation multiplication and tangling [9]. The extensive formation of dislocation tangles (highlighted by red arrows in Fig. 10d) and frequent cross-slip contribute directly to sustained strain-hardening, even at high deformation stages, effectively delaying fracture initiation and enabling the concurrent achievement of high strength and ductility [65,66]. These observations align closely with recent findings on AM-processed Ti alloys, where rapid solidification effectively suppresses micro-segregation, refines the microstructure, and promotes uniform deformation by enhancing dislocation interaction and multiplication [67,68]. This distinctive dislocation behavior in the AM Ti-6Al sample underlies its ability to achieve superior combination of strength and ductility compared to conventional cast alloys.

4.2.2. *Crack propagation*

Based on the observed dislocation behaviors, the as-cast Ti-6Al sample tends to localize strain more readily, thereby facilitating crack propagation along specific crystallographic directions. To gain further insight into the influence of dislocation behavior on mechanical properties, we investigated the crystallographic mechanisms of crack propagation in both as-cast and AM Ti-6Al samples.

EBSD analysis was performed on regions adjacent to the fracture surface of both samples (Fig. 11a1 and b1). In the as-cast Ti-6Al sample, interlamellar cracks are predominant, propagating primarily along the large plate-like grains. Within these grains, numerous microcracks are observed near the prominent interlamellar cracks, propagating along specific crystallographic orientations, as schematically delineated by red dotted lines and indicated by red arrows in the IPF and KAM maps (Fig. 11a2–a3). This behavior supports the hypothesis that planar dislocation activity, constrained to a single slip plane, leads to strain localization and preferential propagation of microcracks along specific planes, ultimately resulting in premature failure [69,70].

In contrast, although interlamellar cracks are also present in the AM Ti-6Al sample (Fig. 11b2), the microcracks near the dominant large interlamellar cracks propagate in multiple directions, as evidenced by the elevated KAM values, schematically delineated by red dotted lines and marked by red arrows Fig. 11b3. This observation aligns with the dislocation behavior noted in the TEM images and suggests that the

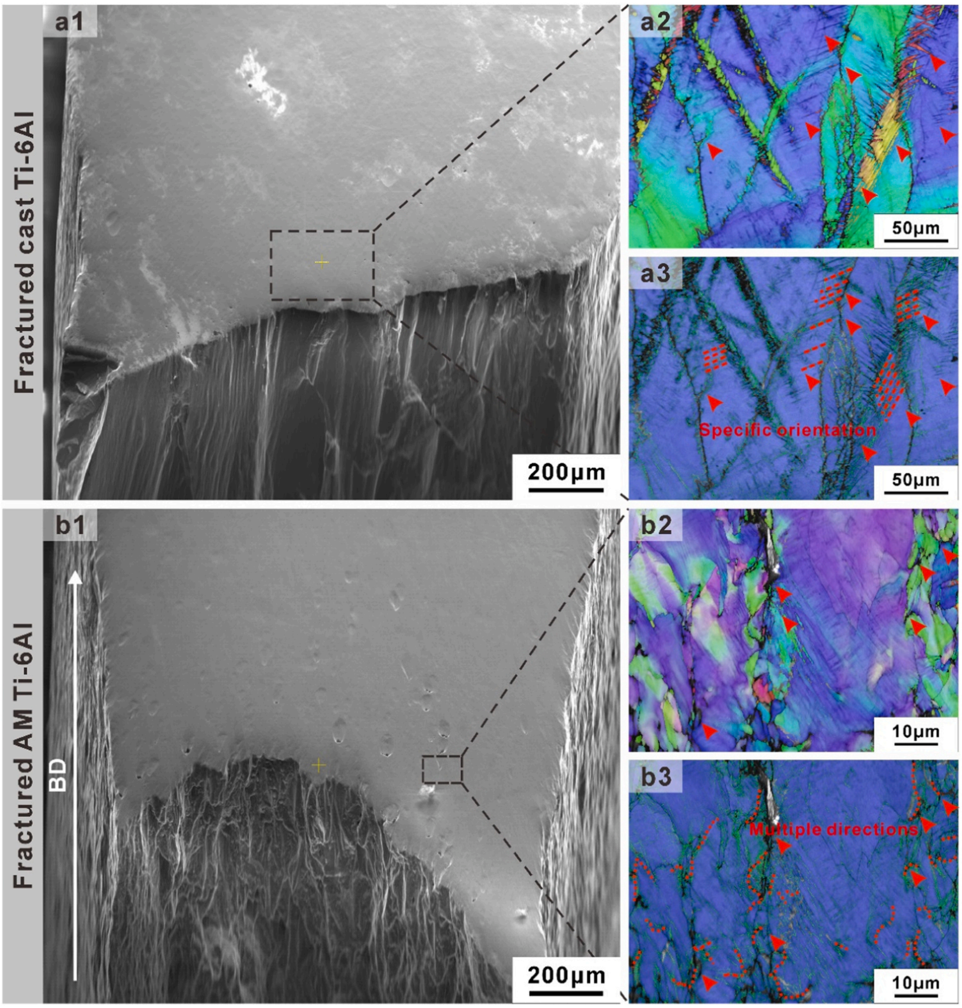

Fig. 11. EBSD analysis of crack propagation in the as-cast and AM Ti-6Al samples. (a1, b1) SEM images showing the examined areas of the as-cast and AM Ti-6Al samples. (a2, a3) IPF and KAM maps of the as-cast sample, highlighting dominant interlamellar cracks, with numerous microcracks propagating along specific crystallographic orientations within plate-like grains. (b2, b3) IPF and KAM maps of the AM sample illustrating dominant interlamellar cracks, with microcracks propagating in multiple directions.

activation of multiple slip systems in the AM Ti-6Al sample not only facilitates dislocation entanglement during deformation but also impedes the propagation of microcracks along a single direction. This combined effect contributes to the simultaneous enhancement of both strength and ductility in the AM Ti-6Al sample [71,72].

The fractographic analyses of the as-cast and AM Ti-6Al samples reveal significant differences in fracture mechanisms, directly correlated with their respective microstructural evolutions (Fig. 12). The as-cast Ti-6Al sample exhibits predominantly brittle fracture features, evident by sharp, staircase-like cleavage facets with smooth contours (Fig. 12a1–a3). These columnar-shaped facets (highlighted by blue dotted lines in Fig. 12a3) align closely with the underlying α-columnar grain structures, signifying a predominantly trans-granular cleavage fracture. This brittle behavior is largely attributed to segregation-induced embrittlement resulting from solute partitioning inherent in conventional casting processes [23]. Specifically, micro-segregation leads localized, solute-enriched regions, significantly weakening grain boundaries and providing preferential pathways for rapid crack initiation and propagation [24]. The absence of dimples and the distinctly planar nature of these cleavage facets further confirms the limited plastic deformation preceding fracture, a characteristic feature of embrittlement arising from the inhomogeneities. Such segregation-induced defects act as intrinsic stress concentrators, diminishing fracture toughness and enhancing susceptibility to brittle failure.

In contrast, the AM Ti-6Al sample demonstrates a pronounced ductile fracture mode, characterized by a classic cup-and-cone fracture surface accompanied by significant necking (Fig. 12b1). Higher magnification observations (Fig. 12b2–b3) reveal densely distributed, deep and equiaxed dimples, indicative of substantial plastic deformation achieved through void nucleation, growth, and coalescence. This enhanced ductility is primarily attributed to the refined, segregation-free microstructure attained through rapid solidification conditions characteristic of additive manufacturing. The inherently high cooling rates during AM effectively suppress solute partitioning, thereby eliminating embrittling segregation and promoting chemical homogeneity. Such a homogenized microstructure facilitates more uniform strain distribution, while the refined grain morphology provides enhanced grain boundary strength, collectively hindering crack initiation and propagation [73,74]. The clear transition from brittle cleavage in the as-cast sample to pronounced ductile dimpling in the AM-produced material highlights the critical role of AM in mitigating segregation embrittlement, ultimately enhancing mechanical performance and fracture resilience.

5. Conclusions

The comparison of the microstructural and mechanical properties of Ti-6Al alloys fabricated through both as-cast and AM processes has elucidated significant differences attributed to the distinct manufacturing techniques employed. The key findings are as follows:

(1) The AM Ti-6Al samples exhibited significantly improved tensile strength and ductility compared to their as-cast counterparts. Specifically, the AM Ti-6Al samples achieved a 90 % improvement in YS, an 80 % increase in UTS, and nearly a 100 % enhancement in elongation to failure compared to the as-cast samples. These results strongly indicate that even low-alloy α-Ti alloys can achieve superior properties, making them a promising candidate for commercial applications utilizing AM methods.

(2) The enhancement in YS is directly associated with the microstructural advantages observed in the AM samples, including the presence of fine basketweave grains that effectively impede dislocation movement during deformation and enhance dislocation strengthening. Additionally, the increased dislocation densities within the fine basketweave grains also contribute to the YS, primarily as a result of the rapid cooling rates and complex thermal history characteristic of AM processes.

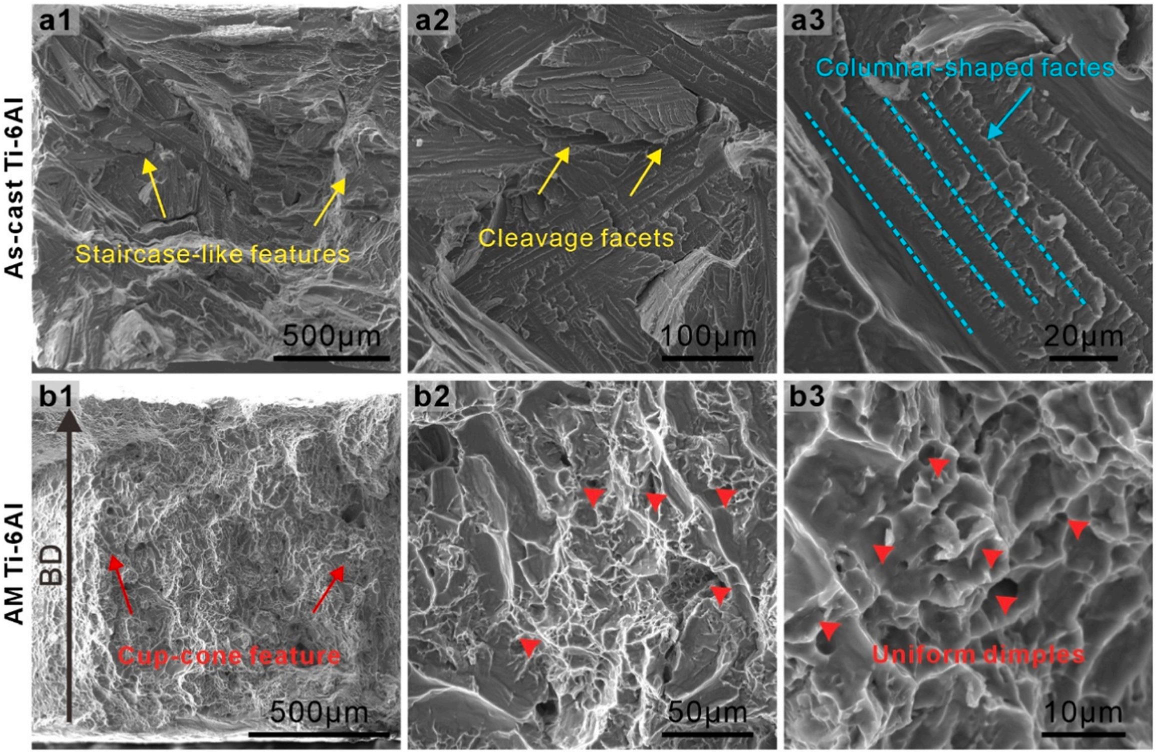

Fig. 12. Fracture morphologies of as-cast and AM Ti-6Al tensile samples. (a1) Overview of the fracture surface of the as-cast Ti-6Al tensile sample. (a2, a3) Higher-magnification images showing staircase-like cleavage facets indicative of brittle fracture. (b1) Overview of the fracture surface of the AM Ti-6Al tensile sample. (b2, b3) Enlarged views revealing a high density of deep, equiaxed dimples, characteristic of ductile fracture.

(3) The superior ductility observed in the AM Ti-6Al samples can be attributed to differences in dislocation behavior, with the as-cast samples predominantly exhibiting planar slip and the AM samples characterized by wavy slip. This variation in dislocation behavior is linked to differences in cooling rates: the low cooling rate of the as-cast samples promotes SRO, facilitating planar slip, while the high cooling rate associated with the additive manufacturing process allows for a supersaturated solid solution that encourages wavy slip. The intricate dislocation structure resulting from wavy slip enhances strain hardening and plastic deformation capacity. Furthermore, the dislocation tangles in the AM Ti-6Al samples act as Frank-Read sources, promoting the formation of dislocation tangles and thereby enhancing the material's ability to undergo deformation without experiencing premature failure.

(4) The findings of this study underscore the potential of AM to produce low-alloy α-Ti with enhanced mechanical properties through the strategic manipulation of microstructure. The inherent advantages of AM, including rapid cooling rates and complex thermal histories, play a crucial role in improving ductility and strength. These enhancements offer promising avenues for the development of high-performance materials suitable for a wide range of applications.

CRediT authorship contribution statement

Shi Hengchao: Investigation. **Zhang Dongdong:** Methodology, Investigation. **Ren Chuanxi:** Methodology, Investigation. **Liu Qi:** Validation, Methodology. **Chen Xuanlai:** Software, Methodology. **Sun Haoran:** Writing – review & editing, Methodology. **Xiang Dingding:** Writing – review & editing, Validation. **Dan Xingdong:** Writing – original draft, Methodology, Investigation, Data curation. **Chen Zibin:** Writing – review & editing, Project administration, Funding acquisition, Conceptualization. **Liu Zhiyuan:** Writing – review & editing, Investigation. **Song Ni:** Writing – review & editing, Supervision, Formal analysis. **Chan K.C.:** Writing – review & editing, Supervision.

Declaration of Competing Interest

The authors declare that they have no known competing financial interests or personal relationships that could have appeared to influence the work reported in this paper.

Acknowledgements

The authors gratefully acknowledge the financial support from the Research Committee of The Hong Kong Polytechnic University (PolyU), the PolyU Research and Innovation Office (Project code: BBR5, CD9E, and UARQ), the Shenzhen Municipal Science and Technology Innovation Commission (Project code: ZGMH), and the State Key Laboratories in Hong Kong, funded by the Innovation and Technology Commission of the Government of the Hong Kong Special Administrative Region, China. The authors would also like to extend their sincere thanks to Dr. Ruien Hu and Mr. Kenneth K.H. Cheng from the Department of Industrial and Systems Engineering, The Hong Kong Polytechnic University, for their assistance with sample preparation.

Data Availability

Data will be made available on request.

References

[1] K. Ma, H. Wen, T. Hu, T.D. Topping, D. Isheim, D.N. Seidman, E.J. Lavernia, J. M. Schoenung, Mechanical behavior and strengthening mechanisms in ultrafine grain precipitation-strengthened aluminum alloy, Acta Mater. 62 (2014) 141–155.

[2] C. Veiga, J.P. Davim, A. Loureiro, Properties and applications of titanium alloys: a brief review, Rev. Adv. Mater. Sci. 32 (2) (2012) 133–148.

[3] C. Choi, H.J. Kim, Y.-T. Lee, Y.-W. Kim, C.S. Lee, Effects of microstructural parameters on the fatigue crack growth of fully lamellar γ-TiAl alloys, Mater. Sci. Eng. A 329 (2002) 545–556.

[4] R. Imayev, V. Imayev, M. Oehring, F. Appel, Microstructural evolution during hot working of Ti aluminide alloys: influence of phase constitution and initial casting texture, Metall. Mater. Trans. A 36 (3) (2005) 859–867.

[5] Y.-W. Kim, D.M. Dimiduk, Progress in the understanding of gamma titanium aluminides, Jom 43 (8) (1991) 40–47.

[6] X. Dan, C. Ren, Z. Song, S. Waqar, D. Zhang, M. Wang, Q. Liu, Y. Sun, X. Chen, W. Jiang, Exceptional strength and ductility in heterogeneous multi-gradient TiAl alloys through additive manufacturing, Acta Mater. 281 (2024) 120395.

[7] T. Song, Z. Chen, X. Cui, S. Lu, H. Chen, H. Wang, T. Dong, B. Qin, K.C. Chan, M. Brandt, Strong and ductile titanium–oxygen–iron alloys by additive manufacturing, Nature 618 (7963) (2023) 63–68.

[8] S.S. Youssef, X. Zheng, M. Qi, Y. Ma, S. Huang, J. Qiu, S. Zheng, J. Lei, R. Yang, Effects of Al content and $\alpha2$ precipitation on the fatigue crack growth behaviors of binary Ti–Al alloys, Mater. Sci. Eng. A 819 (2021) 141513.

[9] Y. Chong, R. Zhang, M.S. Hooshmand, S. Zhao, D.C. Chrzan, M. Asta, J. Morris, Jr, A.M. Minor, Elimination of oxygen sensitivity in α-titanium by substitutional alloying with Al, Nat. Commun. 12 (1) (2021) 6158.

[10] W. Jiang, R. Li, J. He, S. Ni, L. Wang, Z. Chen, Y. Huang, C. Li, J. Yi, M. Song, Nitrogen-doping assisted local chemical heterogeneity and mechanical properties in CoCrMoW alloys manufactured via laser powder bed fusion, Adv. Powder Mater. 3 (5) (2024) 100217.

[11] F. Froes, B. Dutta, The additive manufacturing (AM) of titanium alloys, Adv. Mater. Res. 1019 (2014) 19–25.

[12] M. Molitch-Hou, Overview of additive manufacturing process. Additive Manufacturing, Elsevier, 2018, pp. 1–38.

[13] Q. Liu, C. Ren, Z. Song, X. Dan, J. Ju, T. Yang, S. Ni, J. Lu, L. Liu, J. Pan, High-strength and high-conductivity additively manufactured Cu-O alloy enabled by cellular microstructure, Addit. Manuf. (2024) 104244.

[14] B. Dong, Z. Wang, H. Zhu, O. Muránsky, Z. Qiu, C. Shen, Z. Pan, H. Li, Low neutron cross-section FeCrVTiNi based high-entropy alloys: Design, Addit. Manuf. Charact. (2022).

[15] Z. Liu, D. Zhao, P. Wang, M. Yan, C. Yang, Z. Chen, J. Lu, Z. Lu, Additive manufacturing of metals: microstructure evolution and multistage control, J. Mater. Res. Technol. 100 (2022) 224–236.

[16] N.A. Zumdick, L. Jauer, L.C. Kersting, T.N. Kutz, J.H. Schleifenbaum, D. Zander, Additive manufactured WE43 magnesium: a comparative study of the microstructure and mechanical properties with those of powder extruded and as-cast WE43, Mater. Charact. 147 (2019) 384–397.

[17] M. Cabibbo, R. Montanari, A. Pola, M. Tocci, A. Varone, Mechanical spectroscopy study of as-cast and additive manufactured AlSi10Mg, J. Alloy. Compd. 914 (2022) 165361.

[18] J.C. Pereira, E. Gil, L. Solaberrieta, M. San Sebastián, Y. Bilbao, P.P. Rodríguez, Comparison of AlSi7Mg0. 6 alloy obtained by selective laser melting and investment casting processes: microstructure and mechanical properties in as-built/as-cast and heat-treated conditions, Mater. Sci. Eng. A 778 (2020) 139124.

[19] J. Zeng, Y. Yang, H. Peng, P. Wang, C. Liu, Z. Chen, W. Chen, X. Liu, Y. Wu, Z. Liu, Additive manufacturing of high entropy shape memory alloy with outstanding properties through multi-remelting in-situ alloying, Addit. Manuf. (2024) 104253.

[20] W. Zhang, X. Shang, S. Chen, L. Zhang, Comparison of microstructural characteristics and mechanical properties of the high-strength low-alloy steels fabricated by wire arc additive manufacturing versus conventional casting, Mater. Sci. Eng. A 885 (2023) 145593.

[21] M. Avateffazeli, P. Carrion, B. Shachi-Amirkhiz, H. Pirgazi, M. Mohammadi, N. Shamsaei, M. Haghshenas, Correlation between tensile properties, microstructure, and processing routes of an Al–Cu–Mg–Ag–TiB2 (A205) alloy: additive manufacturing and casting, Mater. Sci. Eng. A 841 (2022) 142989.

[22] J. Kang, R. Li, M. Wang, D. Zheng, P. Niu, T. Yuan, Comparative analysis of microstructure and mechanical properties in FeMnAlNi alloys fabricated via casting and additive manufacturing, Mater. Sci. Eng. A 915 (2024) 147216.

[23] A. Mitchell, A. Kawakami, S. Cockcroft, Segregation in titanium alloy ingots, High. Temp. Mater. Process 26 (1) (2007) 59–78.

[24] A. Mitchell, Melting, casting and forging problems in titanium alloys, Mater. Sci. Eng. A 243 (1-2) (1998) 257–262.

[25] S. Huang, J. Zhang, Y. Ma, S. Zhang, S.S. Youssef, M. Qi, H. Wang, J. Qiu, D. Xu, J. Lei, Influence of thermal treatment on element partitioning in $\alpha+\beta$ titanium alloy, J. Alloy. Compd. 791 (2019) 575–585.

[26] M.H. Mosallanejad, B. Niroumand, A. Aversa, A. Saboori, In-situ alloying in laser-based additive manufacturing processes: a critical review, J. Alloy. Compd. 872 (2021) 159567.

[27] W. Zhai, W. Zhou, S.M.L. Nai, Grain refinement of 316L stainless steel through in-situ alloying with Ti in additive manufacturing, Mater. Sci. Eng. A. 840 (2022) 142912.

[28] R. Xi, H. Jiang, G. Li, S. Kustov, Z. Zhang, H. Wei, Z. Liu, G. Zhao, J. Van Humbeeck, X. Wang, In-situ alloying of NiTiNb ternary shape memory alloys via laser powder bed fusion using pre-alloyed NiTi and elemental Nb powders: microstructure, phase transformation behavior and functional properties, Addit. Manuf. 79 (2024) 103933.

[29] Y. Chong, M. Poschmann, R. Zhang, S. Zhao, M.S. Hooshmand, E. Rothchild, D. L. Olmsted, J. Morris, Jr, D.C. Chrzan, M. Asta, Mechanistic basis of oxygen sensitivity in titanium, Sci. Adv. 6 (43) (2020) eabc4060.

[30] A. Fitzner, D.L. Prakash, J.Q. Da Fonseca, M. Thomas, S.-Y. Zhang, J. Kelleher, P. Manuel, M. Preuss, The effect of aluminium on twinning in binary alpha-titanium, Acta Mater. 103 (2016) 341–351.

[31] H. Yu, S. Cao, S.S. Youssef, Y.-J. Ma, J.-F. Lei, Y. Qi, Q.-M. Hu, R. Yang, Generalized stacking fault energies and critical resolved shear stresses of random α-Ti-Al alloys from first-principles calculations, J. Alloy. Compd. 850 (2021) 156314.

[32] L. Bolzoni, S. Raynova, F. Yang, Strengthening mechanisms of Ti via Al addition, J. Alloy. Compd. 820 (2020) 153447.

[33] I. Ohnuma, Y. Fujita, H. Mitsui, K. Ishikawa, R. Kainuma, K. Ishida, Phase equilibria in the Ti–Al binary system, Acta Mater. 48 (12) (2000) 3113–3123.

[34] B. Rajesh Kumar, B. Hymavathi, X-ray peak profile analysis of solid-state sintered alumina doped zinc oxide ceramics by Williamson–Hall and size-strain plot methods, J. Asian Ceram. Soc. 5 (2) (2017) 94–103.

[35] T. Ahmed, H. Rack, Phase transformations during cooling in α+β titanium alloys, Mater. Sci. Eng. A. 243 (1-2) (1998) 206–211.

[36] C. Ng, M. Bermingham, M. Dargusch, Controlling grain size, morphology and texture in additively manufactured β-titanium alloy with super transus hot isostatic pressing, Addit. Manuf. 59 (2022) 103176.

[37] S. Tedman-Jones, S. McDonald, M. Bermingham, D. StJohn, M. Dargusch, Investigating the morphological effects of solute on the β-phase in as-cast titanium alloys, J. Alloy. Compd. 778 (2019) 204–214.

[38] J. Zhang, Y. Liu, M. Bayat, Q. Tan, Y. Yin, Z. Fan, S. Liu, J.H. Hattel, M. Dargusch, M.-X. Zhang, Achieving high ductility in a selectively laser melted commercial pure-titanium via in-situ grain refinement, Scr. Mater. 191 (2021) 155–160.

[39] G.-H. Zhao, X. Liang, B. Kim, P. Rivera-Díaz-del-Castillo, Modelling strengthening mechanisms in beta-type Ti alloys, Mater. Sci. Eng. A 756 (2019) 156–160.

[40] C. Zhang, X. Bao, D. Zhang, W. Chen, J. Zhang, J. Kuang, G. Liu, J. Sun, Achieving superior strength-ductility balance in a novel heterostructured strong metastable β-Ti alloy, Int. J. Plast. 147 (2021) 103126.

[41] K. Lu, J. Li, Y. Wang, X. Ma, Excellent strength-ductility synergy and corrosion resistance in a metastable high entropy alloy via heterogeneous structure design, J. Alloy. Compd. 941 (2023) 168979.

[42] D. Lesuer, C. Syn, O. Sherby, J. Wadsworth, J. Lewandowski, W. Hunt, Mechanical behaviour of laminated metal composites, Int. Mater. Rev. 41 (5) (1996) 169–197.

[43] D. Li, G. Fan, X. Huang, D.J. Jensen, K. Miao, C. Xu, L. Geng, Y. Zhang, T. Yu, Enhanced strength in pure Ti via design of alternating coarse-and fine-grain layers, Acta Mater. 206 (2021) 116627.

[44] G.-H. Zhao, X. Xu, D. Dye, P.E. Rivera-Díaz-del-Castillo, Microstructural evolution and strain-hardening in TWIP Ti alloys, Acta Mater. 183 (2020) 155–164.

[45] A. Bahador, J. Umeda, R. Yamanoglu, A. Amrin, A. Alhazaa, K. Kondoh, Ultrafine-grain formation and improved mechanical properties of novel extruded Ti-Fe-W alloys with complete solid solution of tungsten, J. Alloy. Compd. 875 (2021) 160031.

[46] Y. Lu, R. Kotoka, J. Ligda, B. Cao, S. Yarmolenko, B. Schuster, Q. Wei, The microstructure and mechanical behavior of Mg/Ti multilayers as a function of individual layer thickness, Acta Mater. 63 (2014) 216–231.

[47] P. Kwasniak, H. Garbacz, Screw dislocation mediated solution strengthening of substitutional α-Ti alloys-First principles investigation, Acta Mater. 141 (2017) 405–418.

[48] S.S. Kumar, B. Pavithra, V. Singh, P. Ghosal, T. Raghu, Tensile anisotropy associated microstructural and microtextural evolution in a metastable beta titanium alloy, Mater. Sci. Eng. A 747 (2019) 1–16.

[49] M. Calcagnotto, D. Ponge, E. Demir, D. Raabe, Orientation gradients and geometrically necessary dislocations in ultrafine grained dual-phase steels studied by 2D and 3D EBSD, Mater. Sci. Eng. A 527 (10-11) (2010) 2738–2746.

[50] Z. Yan, D. Wang, X. He, W. Wang, H. Zhang, P. Dong, C. Li, Y. Li, J. Zhou, Z. Liu, Deformation behaviors and cyclic strength assessment of AZ31B magnesium alloy based on steady ratcheting effect, Mater. Sci. Eng. A. 723 (2018) 212–220.

[51] C. Pande, K. Cooper, Nanomechanics of Hall–Petch relationship in nanocrystalline materials, Prog. Mater. Sci. 54 (6) (2009) 689–706.

[52] T. Zhang, J. Zhu, T. Yang, J. Luan, H. Kong, W. Liu, B. Cao, S. Wu, D. Wang, Y. Wang, A new α+ β Ti-alloy with refined microstructures and enhanced mechanical properties in the as-cast state, Scr. Mater. 207 (2022) 114260.

[53] Y. Dong, Y. Li, S. Zhou, Y. Zhou, M. Dargusch, H. Peng, M. Yan, Cost-affordable Ti-6Al-4V for additive manufacturing: powder modification, compositional modulation and laser in-situ alloying, Addit. Manuf. 37 (2021) 101699.

[54] F. Zhang, M. Yang, A.T. Clare, X. Lin, H. Tan, Y. Chen, Microstructure and mechanical properties of Ti-2Al alloyed with Mo formed in laser additive manufacture, J. Alloy. Compd. 727 (2017) 821–831.

[55] Y. Liu, J. Ren, S. Guan, C. Li, Y. Zhang, S. Muskeri, Z. Liu, D. Yu, Y. Chen, K. An, Microstructure and mechanical behavior of additively manufactured CoCrFeMnNi high-entropy alloys: laser directed energy deposition versus powder bed fusion, Acta Mater. 250 (2023) 118884.

[56] R. Zhang, S. Zhao, C. Ophus, Y. Deng, S.J. Vachhani, B. Ozdol, R. Traylor, K. Bustillo, J. Morris Jr, D.C. Chrzan, Direct Imaging of Short-range Order and Its Relationship to Deformation in Ti-6Al, Sci. Adv 5.

[57] D.C. Pagan, P.A. Shade, N.R. Barton, J.-S. Park, P. Kenesei, D.B. Menasche, J. V. Bernier, Modeling slip system strength evolution in Ti-7Al informed by in-situ grain stress measurements, Acta Mater. 128 (2017) 406–417.

[58] P. Kwasniak, S. Delannoy, F. Prima, E. Clouet, Competition between prismatic and basal slip in hexagonal titanium–aluminum alloys with short-range order, Mater. Res. Lett. 11 (6) (2023) 407–413.

[59] T. Neeraj, M. Mills, Short-range order (SRO) and its effect on the primary creep behavior of a Ti–6wt% Al alloy, Mater. Sci. Eng. A. 319 (2001) 415–419.

[60] H. Weng, Q. Wang, Y. Ma, D. Xu, S. Huang, M. Qi, J. Qiu, J. Lei, R. Yang, Effect of Al content on the fracture toughness and deformation behavior of Ti-Al binary alloys, Mater. Sci. Eng. A. 911 (2024) 146914.

[61] D. Truax, C. McMahon, Plastic behavior of titanium-aluminum alloys, Mater. Sci. Eng. 13 (2) (1974) 125–139.

[62] N. Takata, M. Liu, H. Kodaira, A. Suzuki, M. Kobashi, Anomalous strengthening by supersaturated solid solutions of selectively laser melted Al–Si-based alloys, Addit. Manuf. 33 (2020) 101152.

[63] J. Yaokawa, K. Oh-ishi, S. Dong, M. Hara, T. Masutani, H. Sato, Dimensional changes induced by precipitation of supersaturated solid solution Si in selectively laser-melted AlSi10Mg alloy during heat treatment, Mater. Charact. 182 (2021) 111533.

[64] J. Williams, A. Sommer, P. Tung, The influence of oxygen concentration on the internal stress and dislocation arrangements in α titanium, Metall. Mater. Trans. B 3 (1972) 2979–2984.

[65] X.-Q. Wang, W.-Z. Han, Oxygen-gradient titanium with high strength, strain hardening and toughness, Acta Mater. 246 (2023) 118674.

[66] J. Chen, Y. Han, Z. Wei, S. Li, Z. Sun, L. Zhang, G. Huang, J. Le, D. Zhang, W. Lu, Heterostructured titanium composites with superior strength-ductility synergy via controllable bimodal grains and< c+ a> dislocation activity, Mater. Res. Lett. 11 (10) (2023) 863–871.

[67] Y. Dong, J. Tang, D. Wang, N. Wang, Z. He, J. Li, D. Zhao, M. Yan, Additive manufacturing of pure Ti with superior mechanical performance, low cost, and biocompatibility for potential replacement of Ti-6Al-4V, Mater. Des. 196 (2020) 109142.

[68] Y. Dong, D. Wang, Q. Li, X. Luo, J. Zhang, K.G. Prashanth, P. Wang, J. Eckert, L. Mädler, I.V. Okulov, Strong and ductile titanium via additive manufacturing under a reactive atmosphere, Mater. Today Adv. 17 (2023) 100347.

[69] H. Wang, Q. Zhao, S. Xin, Y. Zhao, W. Zhou, W. Zeng, Microstructural morphology effects on fracture toughness and crack growth behaviors in a high strength titanium alloy, Mater. Sci. Eng. A 821 (2021) 141626.

[70] J. Wang, Y. Zhao, W. Zhou, Q. Zhao, S. Huang, W. Zeng, In-situ investigation on tensile deformation and fracture behaviors of a new metastable β titanium alloy, Mater. Sci. Eng. A 799 (2021) 140187.

[71] Q. Song, C. Sun, Mechanism of crack initiation and early growth of high strength steels in very high cycle fatigue regime, Mater. Sci. Eng. A 771 (2020) 138648.

[72] D. Zhang, J. Zhang, J. Kuang, G. Liu, J. Sun, The B2 phase-driven microstructural heterogeneities and twinning enable ultrahigh cryogenic strength and large ductility in NiCoCr-based medium-entropy alloy, Acta Mater. 233 (2022) 117981.

[73] H. Yang, H. Li, H. Sun, Y. Zhang, X. Liu, M. Zhan, Y. Liu, M. Fu, Anisotropic plasticity and fracture of alpha titanium sheets from cryogenic to warm temperatures, Int. J. Plast. 156 (2022) 103348.

[74] Y. Wu, X. Zhao, Q. Chen, C. Yang, M. Jiang, C. Liu, Z. Jia, Z. Chen, T. Yang, Z. Liu, Strengthening and fracture mechanisms of a precipitation hardening high-entropy alloy fabricated by selective laser melting, Virtual Phys. Prototyp. 17 (3) (2022) 451–467.